Effect of aging treatment on the crushing behavior of aluminum 6061 alloy tube

MH Farshidi

Abstract

The effect of heat treatment on the axial crushing behavior of thin-walled aluminum 6061 alloy tubes is studied in this work. For this purpose, thin-walled grooved specimens were subjected to different aging heat treatments to obtain different work hardening behaviors. Afterward, quasi-static axial compression tests were achieved to evaluate the crushing behavior. Additionally, a finite element method simulation was employed to determine the distributions of stress, strain, and imposed damage during axial compression. Results show that the optimum energy absorption characteristics can be obtained using moderated strain hardening exponent, "n". Low strain hardening exponent results in the fracture of tube during axial compression while high strain hardening exponent causes lowered absorbed energy. On comparing the results of experiments and finite element method simulations, the fracture of tube during axial compression can be predicted using a simple fracture criterion.

Keywords

Energy absorption, plastic hinge, work hardening, thin-walled tube, axisymmetric compression

Date received: 19 September 2013; accepted: 30 January 2014

Introduction

Energy absorption is an important characteristic of materials used in shock load-bearing structures. Examples of these structures can be presented as car structures, ships, and lifts. In these structures, the main goal is minimizing the shock load imposed damage in the main part of structure. For this, the structure must dissipate energy by moderated load before collapse, which can be occurred by friction, plastic deformation, or metal cutting.[1,2] Among these energy dissipation methods, plastic deformation during axial compression is extensively attended due to its high energy absorption capabilities.[3–5] Additionally, tubes have been widely used as the energy dissipating elements due to their high stiffness, low weight, ease of production, and low cost.[3–7]

Axial deformation behavior of tube can be classified into four different modes:[8,9] overall buckling, concertina mode, diamond mode, and simple compression. Among these modes, concertina mode is more desired due to lower load domain and higher mean load. As shown by Andrew,[8] t/D and L/D can extensively affect crushing behavior of tubes during axial compression. Here, t is the tube thickness, D is the tube diameter, and L is the tube length. It is also shown that thin-walled moderated length tubes have higher chance of crushing by concertina mode.[8]

Many attempts have been concentrated on controlling behavior of tubes during axial compression. Mamalis et al.[10–12] have studied the effect of internal and external grooves on the deformation mode of axially compressed tubes. Gupta and Gupta[13] have introduced holes in thin-walled tubes to prevent overall buckling. Hosseinipour and Daneshi[14,15] have introduced a geometry of grooves for circular thin-walled tubes, which causes deformation in concertina mode during axial compression. In this geometry, tube is grooved by the equally distanced internal and external grooves and the depth of grooves is considered as half of tube thickness.

Aluminum alloys are widely used in the energy dissipating elements due to their attractive characteristics such as low density and good strength. As a result, many studies have been conducted on optimizing energy absorption characteristics of aluminum alloy tubes by different techniques such as controlling the tube forming parameters,[16,17] reinforcing the tube by fibers,[18,19] and filling the tube by metal foams.[20,21]

Department of Materials Science and Engineering, Sharif University of Technology, Tehran, Iran

Corresponding author:
MH Farshidi, Department of Materials Science and Engineering, Sharif University of Technology, Azadi Avenue, Tehran, Iran.
Email: mhfarshidi@alum.sharif.edu

Table 1. Chemical composition of used alloy.

Element	Al	Mg	Si	Fe	Cu	Cr
wt%	Base	1.0	0.84	0.3	0.272	0.06

However, fewer studies have been focused on the effect of heat treatment on the energy absorption characteristics of aluminum tubes.

In this work, the effect of heat treatment on the axial compression behavior of thin-walled aluminum 6061 alloy tubes is studied. To do so, the geometry of grooves proposed by Hosseinipour and Daneshi[14,15] is used and different aging treatments are achieved. Finite element method (FEM) simulation is also carried out to investigate the distribution of stress and strain in tube during axial compression. In addition, a simple fracture criterion is applied to predict fracture of tube during axial compression.

Material, process, and experiments

Tube was received in wrought form and cut to 108.5 mm length pieces. The internal and the external diameter of used tube were 61 mm and 67 mm, respectively. The chemical composition of used alloy is shown in Table 1. A group of specimens was kept in as-received condition while others were solution treated in 530 °C for 1 h and then aged in 205 °C for different time durations. Totally, six different heat treatments were obtained as presented below:

1. AR: As received.
2. F0: Solution treated.
3. F5: Solution treated and aged for 5 min.
4. F10: Solution treated and aged for 10 min.
5. F20: Solution treated and aged for 20 min.
6. F80: Solution treated and aged for 80 min.

Tensile tests were achieved for all heat treatments using ASTM E8/M standard tensile samples. In order to introduce needed grooves, specimens were subjected to machining by CNC. Figure 1(a) shows the schematic cross section of grooved specimens. The distance between grooves was 15.5 mm and the depth of groove was 1.5 mm. Quasi-static axial compression tests were carried out at a rate of 1 mm/s.

FEM simulation

In order to analyze the compression behavior of tube and the stress–strain condition in tube during compression, FEM simulation was achieved using ABAQUS 6.9 software. Material behavior was supposed to follow Hollomon[22] work hardening model as presented below
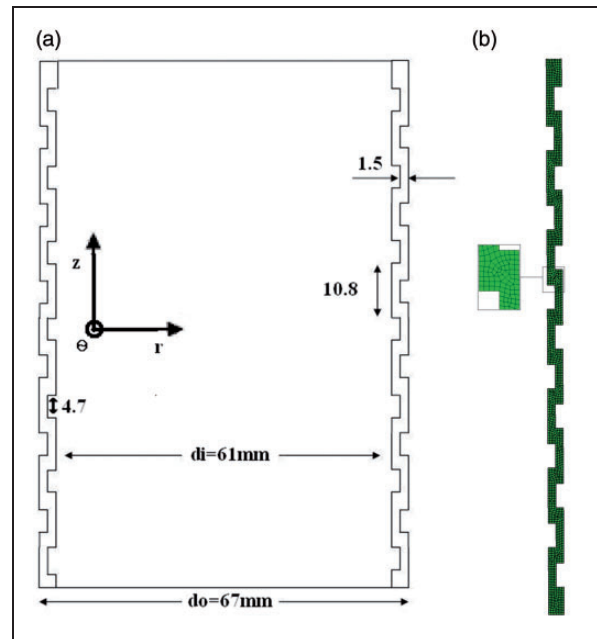
$$\sigma_f = K\varepsilon_p^n \tag{1}$$

Figure 1. (a) Cross section of grooved specimen; (b) meshed cross section of specimen.

where σ_f is equivalent flow stress, ε_p is the equivalent plastic strain, K is the hardening coefficient, and n is the hardening exponent.

The fracture of material was modeled by a state damage variable which increases monotonically in each increment.[23] In this model, the fracture starts when

$$\omega_D = \int \frac{d\varepsilon_p}{\varepsilon_f} = 1 \tag{2}$$

where ω_D is the state damage variable, ε_f is the equivalent fracture strain considering stress–strain condition, and $d\varepsilon_p$ is the variation of equivalent plastic strain in each increment.

Regarding the symmetry of tube, a 2D axisymmetric model was employed to reduce calculation. The applied solution was dynamic explicit. Pressing rams were considered as discrete rigid parts while tube was considered as deformable part. The interaction of surfaces was modeled by penalty contact method. Because the pressing rams and the specimens have smooth surfaces, the frictional effects can be considered as negligible.

Specimen was meshed using approximately 0.375 mm sized CAX4R linear rectangular and CAX3R linear triangular elements. Figure 1(b) illustrates the meshed specimen. The simulation of axial compression for F10 specimen was also repeated with 0.25 mm sized elements. Comparing the results of two simulations of F10 specimen, the mesh sensitivity of applied model was evaluated as negligible. For example, the amount of compression load difference is less than 2.5% between two simulations.

Results and discussion

Figure 2 compares the stress–strain curves of samples with different treatments. Figure 3 shows the variation of yield strength (YS), ultimate tensile strength (UTS), and elongation (El) of samples by aging time. As can be seen in Figures 2 and 3, the strength increases and the elongation decreases by increasing aging time. In addition, an impressive increscent in YS and relatively extensive decrease in El occurs between 10 and 20 min of aging time. Table 2 shows the hardening parameters of samples with different treatments. As can be seen, the hardening exponent decreases during aging time while the hardening coefficient remains nearly constant during aging time. An extensive decrease in the hardening exponent occurs between 10 and 20 min
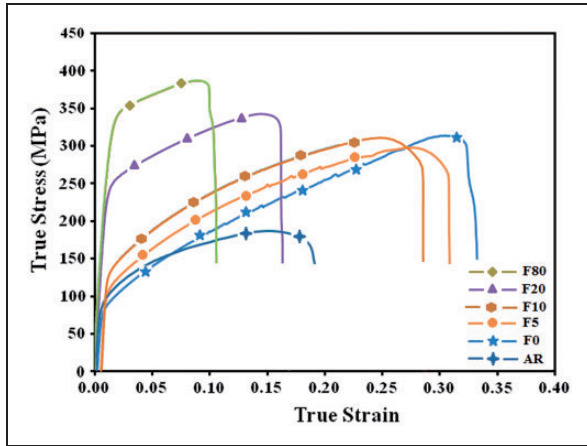

Figure 2. True stress–strain curves for samples with different treatments.

Table 2. Hardening parameters of different heat treated samples.

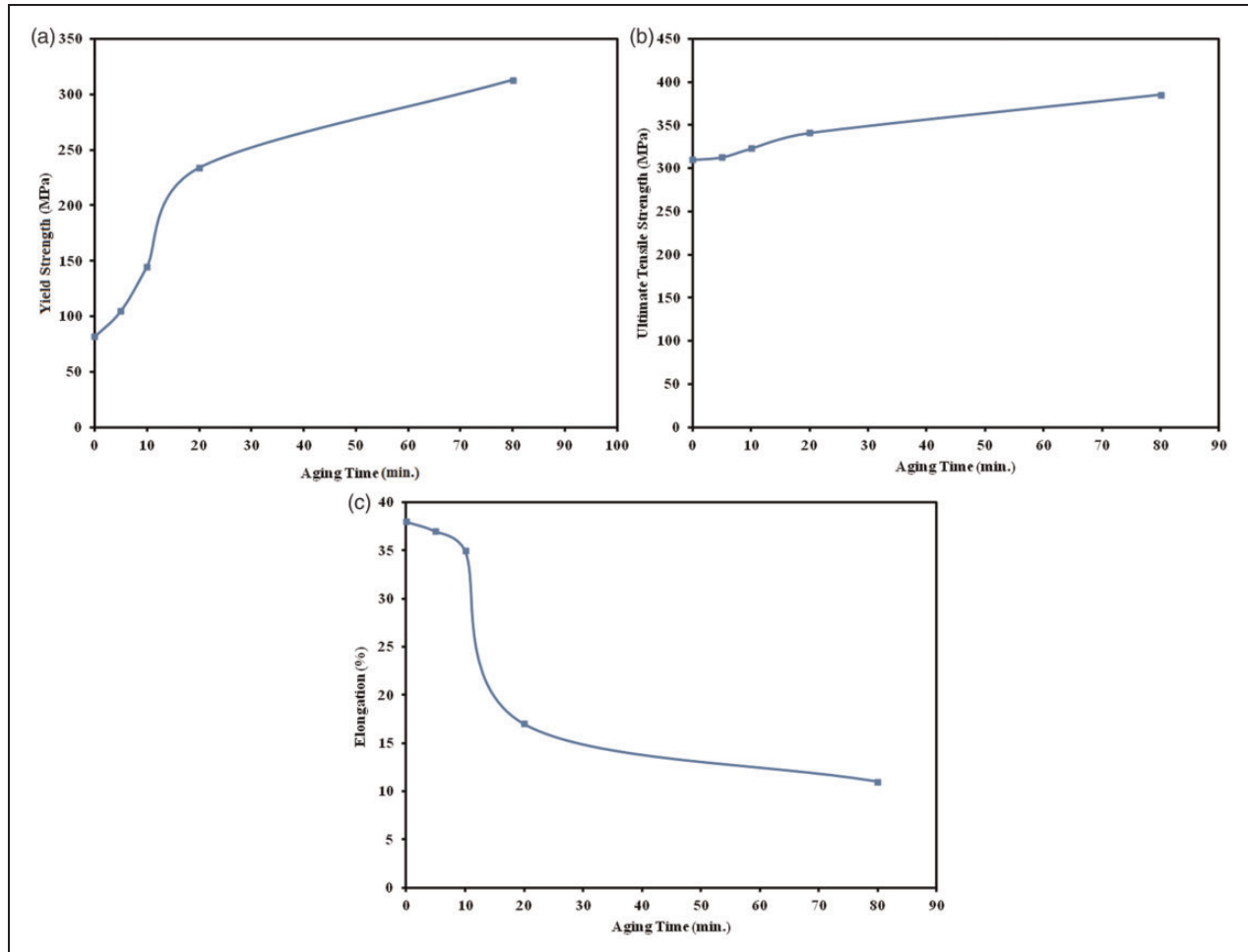| Tensile sample	Hardening exponent (n)	Hardening coefficient (K) (MPa)
AR	0.248	306
F0	0.387	466
F5	0.363	488
F10	0.318	492
F20	0.146	452
F80	0.088	480

Figure 3. Variation of: (a) yield strength; (b) ultimate tensile strength; (c) elongation by aging time.
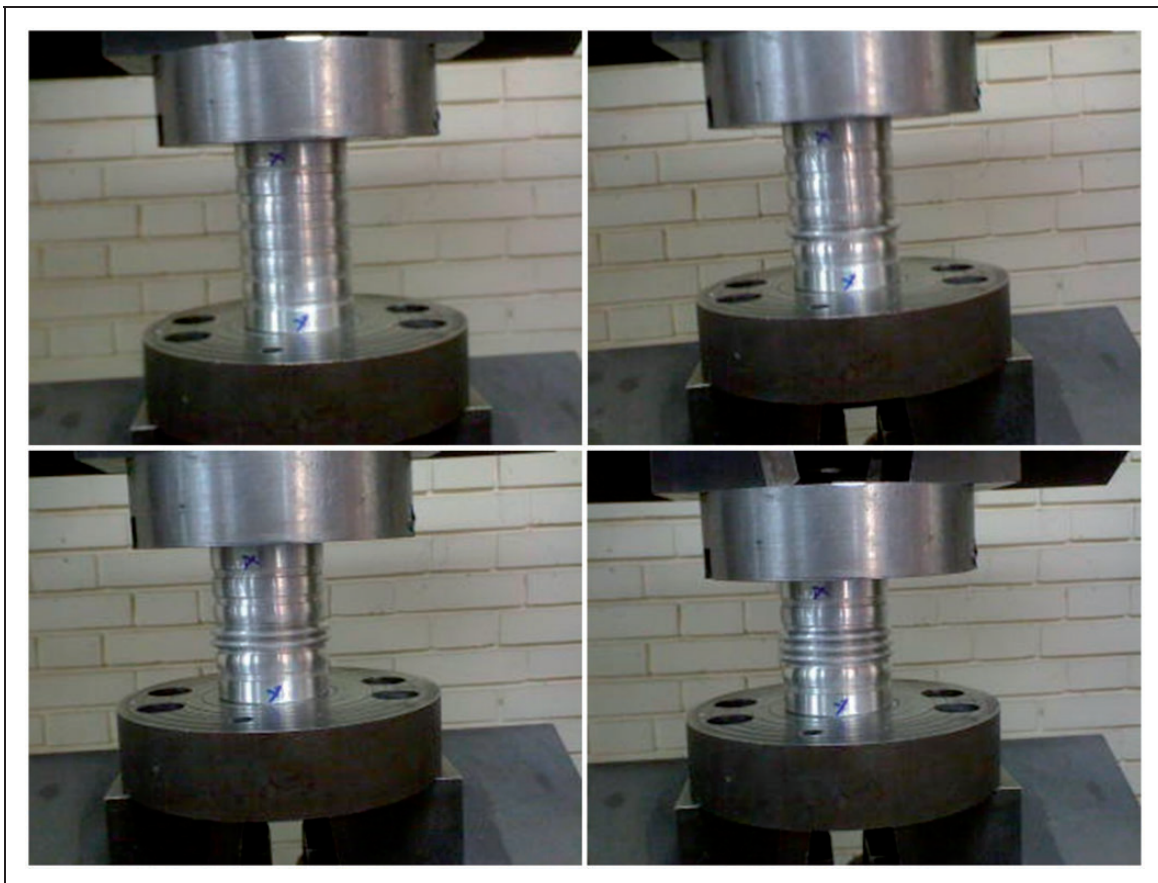
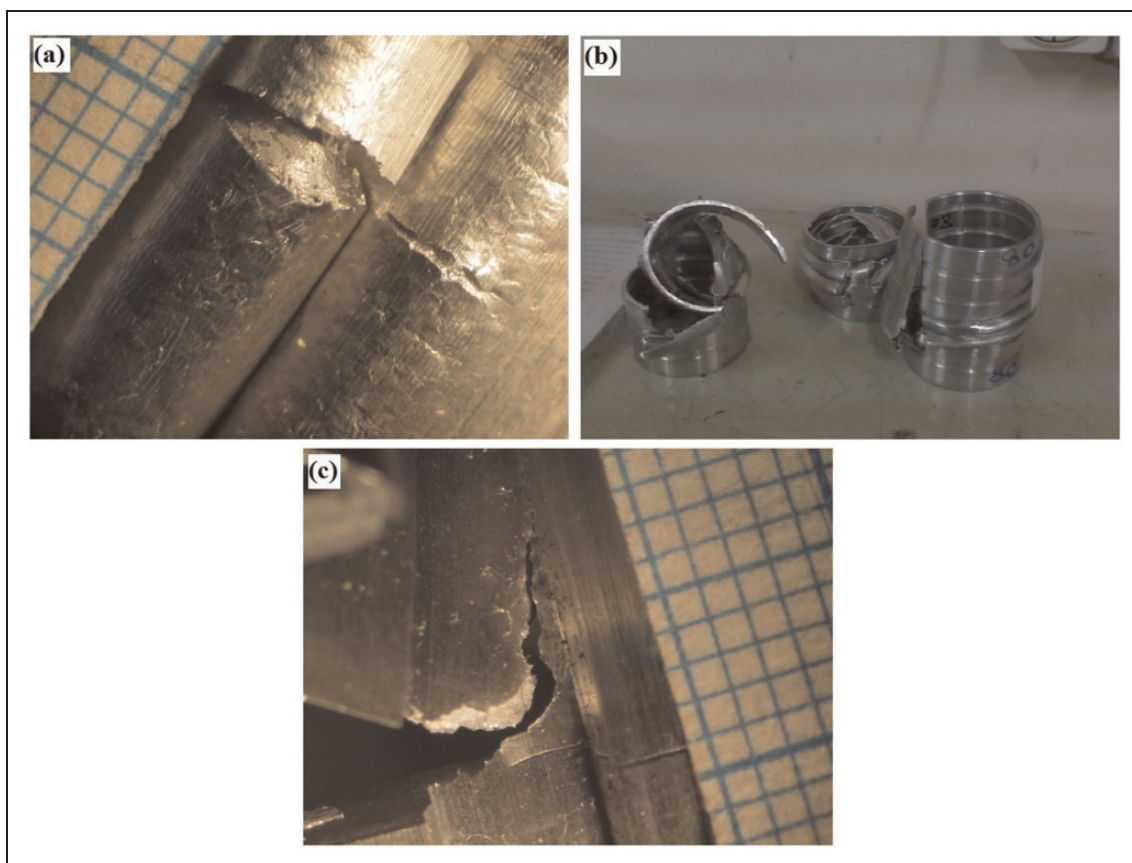**Figure 4.** Steps of axial compression test for AR specimen.

Figure 5. (a) Appearance of macroscopic cracks during axial compression of F20 specimen; (b) and (c) overall fracture of F80 specimen during axial compression. The dimensions of small squares are $1 \times 1 \, mm^2$.
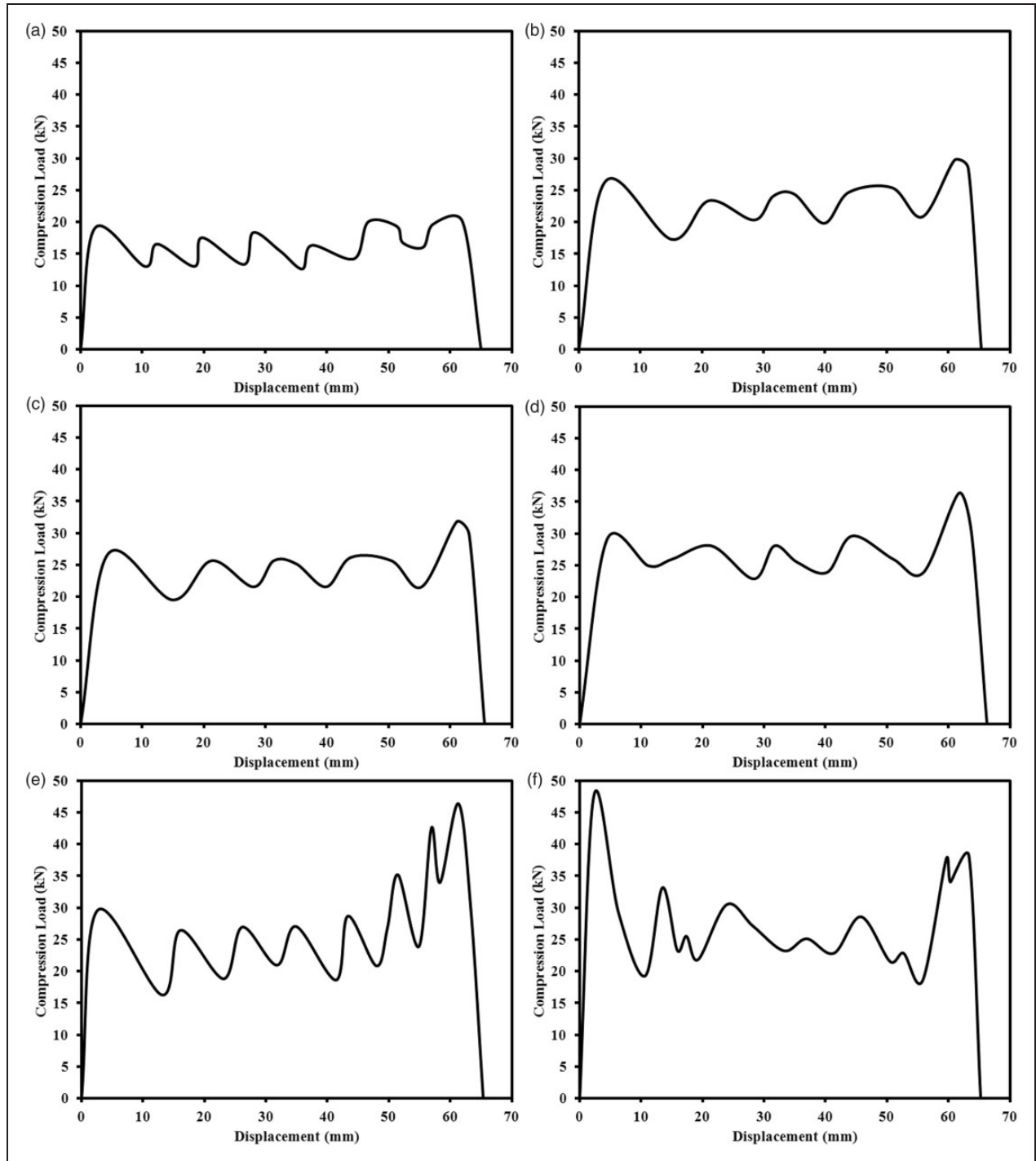
Figure 6. Axial compression load–displacement curves of: (a) AR; (b) F0; (c) F5; (d) F10; (e) F20; and (f) F80.

of aging time. This is related to nucleation and growth of β'' precipitates which are the main hardening precipitates in 6061 alloy.[24]

Figure 4 shows steps of the axial compression test for AR specimen. As shown here, plastic hinges appeared during tube compression, which illustrates that the AR specimen was deformed in concertina mode. Similarly, F0, F5, and F10 specimens were deformed in concertina mode while F20 specimen was crushed by deformation in concertina mode accompanied with small cracks as shown in

Figure 5(a). In comparison, overall fracture of tube occurred during axial compression of F80 specimen as shown in Figure 5(b) and (c).

Load–displacement curves of axial compression test for different specimens are shown in Figure 6. As can be seen, relatively ordered load–displacement curves were obtained during axial compression of AR, F0, F5, and F10 specimens. In these curves, the distances between load maximums are relatively constant and load fluctuates by relatively constant domain. Comparatively, the load–displacement curve of F80

Table 3. Comparison of simulated and experimental obtained compression load for different specimens.

Specimen	AR	F0	F5	F10	F20	F80
Experimental average compression load (P_{av}) (kN)	16.5	21.5	22.9	25.5	26.3	27
Experimental maximum compression load (P_{max}) (kN)	20.5	30.3	32	36.0	46.5	48.4
Experimental load domain (kN)	8	12	12	13	30	31
P_{av}/P_{max}	0.81	0.71	0.72	0.71	0.57	0.56
Simulated average compression load (kN)	17.8	20.5	21.7	24.1	33.7	41.0
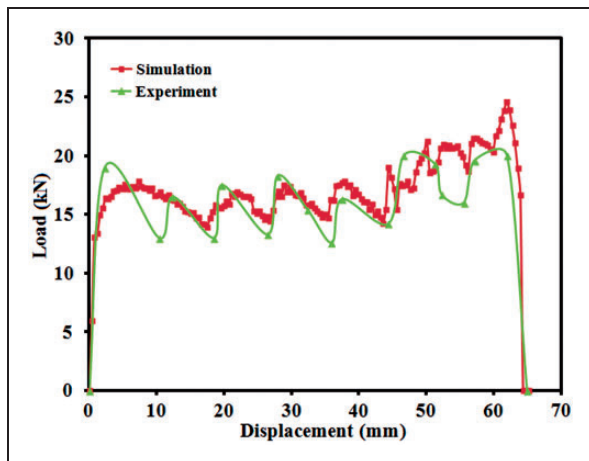
Figure 7. Comparison between experiment and simulation of load–displacement curve of AR specimen.

specimen is disordered as shown in Figure 6(f). In this case, the load decreases drastically after little displacement, which is due to initiation of fracture in F80 specimen during axial compression. The fracture of tube during axial compression is discussed more in descriptions of Figure 10.

In Table 3, the simulated and experimental results of compression load are compared for different specimens. Note that the load domain is calculated from differences of the maximum compression load and the minimum compression load. As can be seen, the average compression load increases rapidly by increasing aging time from 0 to 10 min. However, increasing aging time after 10 min has little effect on the average compression load. In comparison, the compression load domain increases impressively and the P_{av}/P_{max} decreases extensively by increasing aging time to 20 min. This means that the load fluctuation increases impressively, which is not desired for an energy absorbing element.

The simulation results for average compression load of AR, F0, F5, and F10 specimens are near to experiments as can be seen in Table 3. As an illustration, the differences between simulation and experiments are less than 8% and 5% for AR and F0 specimens, respectively. Note that relatively high difference between simulation and experiment for F20 and F80 specimens is due to occurrence of fracture in these specimens which is discussed later. Figure 7 compares the simulated and the experimentally

obtained load–displacement curves of AR specimen. As can be seen, the simulated curve is near to the experimentally obtained curve. Similar results have been observed in comparison of simulated load–displacement curves of F0, F5, F10 specimens with experiments. As a result, it can be concluded that tube deformation can be nearly predicted by the applied simulation.

Considering the aforementioned discussion, one can presume that the age hardening results in the increase of absorbed energy by promotion of work hardening capability. However, it may also cause fracture of tube during compression. As an illustration, the axial compression test causes small cracks in F20 specimen and overall fracture in F80 specimen. This phenomenon is not desired for energy absorbing elements not only because of high fluctuation of load, but also due to low reliability of structure. As a result, ultra-hardened materials are not suitable for energy absorbing elements. Hence, it can be concluded that moderated hardened materials, such as F10 treatment, have most desirable energy absorbing capabilities.

Figure 8 compares the distribution of equivalent strain in specimens after compression to 0.7 of initial height. As can be seen, the equivalent strain is mainly concentrated in hinges appeared during compression. On the other hand, the concurrency of the hinges decreases by increasing the aging time. As an illustration, the hinges in F80 specimen are less concurrent when compared with F0, F5, and F10 specimens. Comparing these results with work hardening exponent of specimens shown in Table 2, it can be concluded that the concurrency of hinges decreases with decreasing work hardening exponent. In other words, in low work hardening exponents, further hinges promote after finishing plastic deformation in first hinge. This increases the concentration of strain in first hinge as shown in Figure 8. As a result, the decrease of work hardening exponent increases the risk of flow localization and fracture of tube during promotion of the first hinge.

Figure 9 shows simulated variation of stress in outer side of the first outer hinge and the first inner hinge in F80 specimen. As shown here, the amount of σ_{rr} and σ_{rz} are negligible compared to $\sigma_{\theta\theta}$ and σ_{zz}. As a result, the stress–strain condition in the outer side of hinges can be estimated similar to sheet stretching. Accordingly, tube fracture can be estimated using sheet stretching fracture criterions.
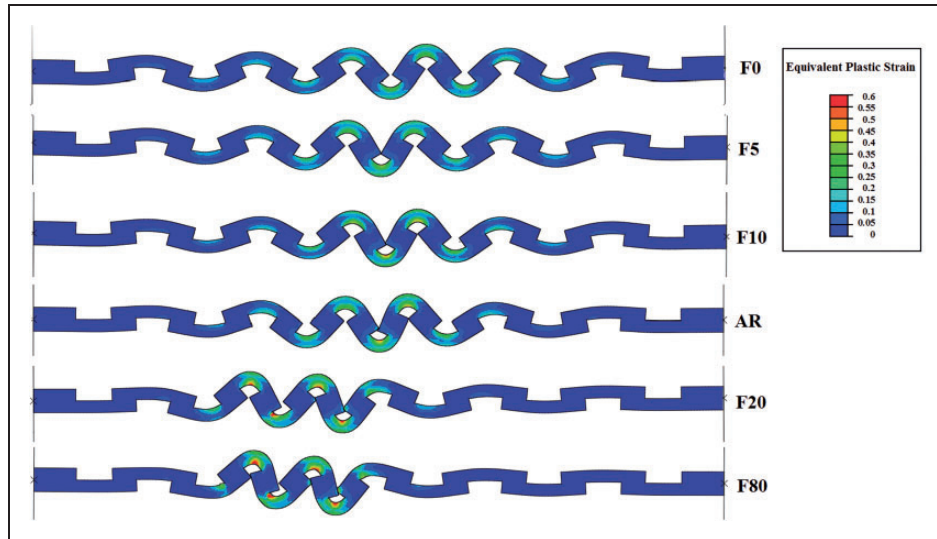
Figure 8. Comparison of equivalent strain distribution and shape of specimens after compression to 0.7 of initial height.
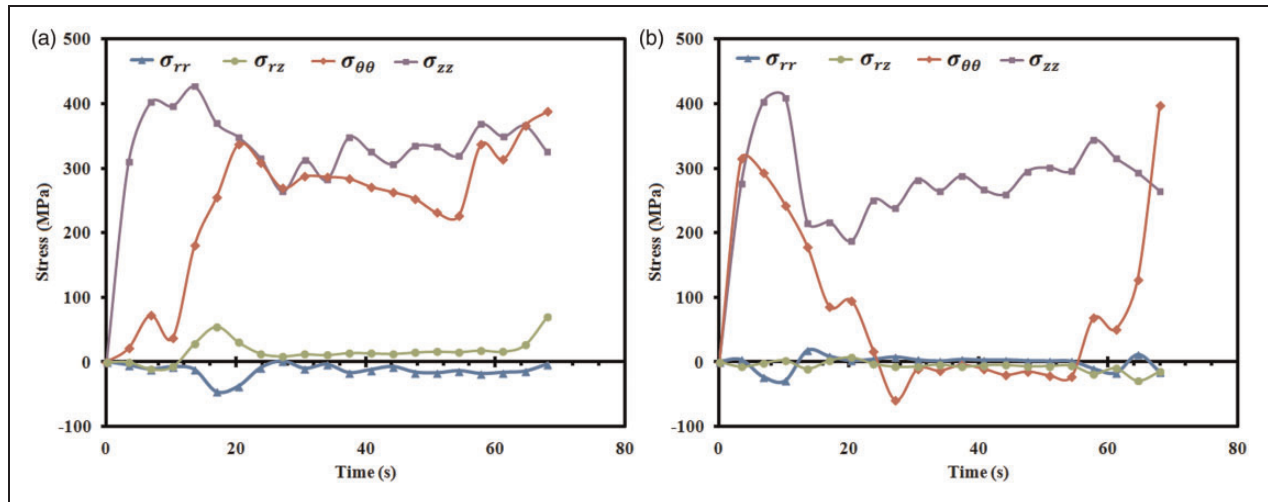

Figure 9. Variation of stress in outer side of: (a) first outer hinge; (b) first inner hinge of F80 specimen.

The equivalent flow localization strain in sheet stretching can be obtained using Swift criterion[25] as follows

$$\varepsilon_{sfl} = \frac{4n\left(1 + \rho + \rho^2\right)^{1.5}}{\sqrt{3}(1 + \rho)(2\rho^2 - \rho + 2)} \qquad (3)$$

where ε_{sfl} is the Swift equivalent flow localization strain and ρ is the stretching ratio defined as

$$\rho = \frac{\varepsilon_2}{\varepsilon_1}$$

Note that the ε_1 and ε_2 are principal strains.

Because the fracture starts immediately after flow localization, the ε_{sfl} can be interpreted as the equivalent fracture strain. Accordingly, the ε_{sfl} can be

substituted as the equivalent fracture strain in equation (2), which presents the Swift damage function.

Figure 10(a) shows the simulated Swift damage in F10 specimen after completion of axial compression test. Note that the fracture is initiated when the swift damage approaches 1 according to definition. As can be seen, the amount of swift damage is less than 1 in F10 specimen. Thus, it can be concluded that no macroscopic crack can be initiated in this specimen, which is in agreement with the experiments discussed earlier. Figure 10(b) compares the simulated swift damage in F20 specimen at different steps. As shown here, the swift damage in the first hinge crosses the critical value of 1 after considerable deformation. Comparatively, propagation of hinges in F20 specimen accompanied with small cracks is shown in Figure 5(a). The swift damage increases rapidly in F80 specimen and crosses the critical value of
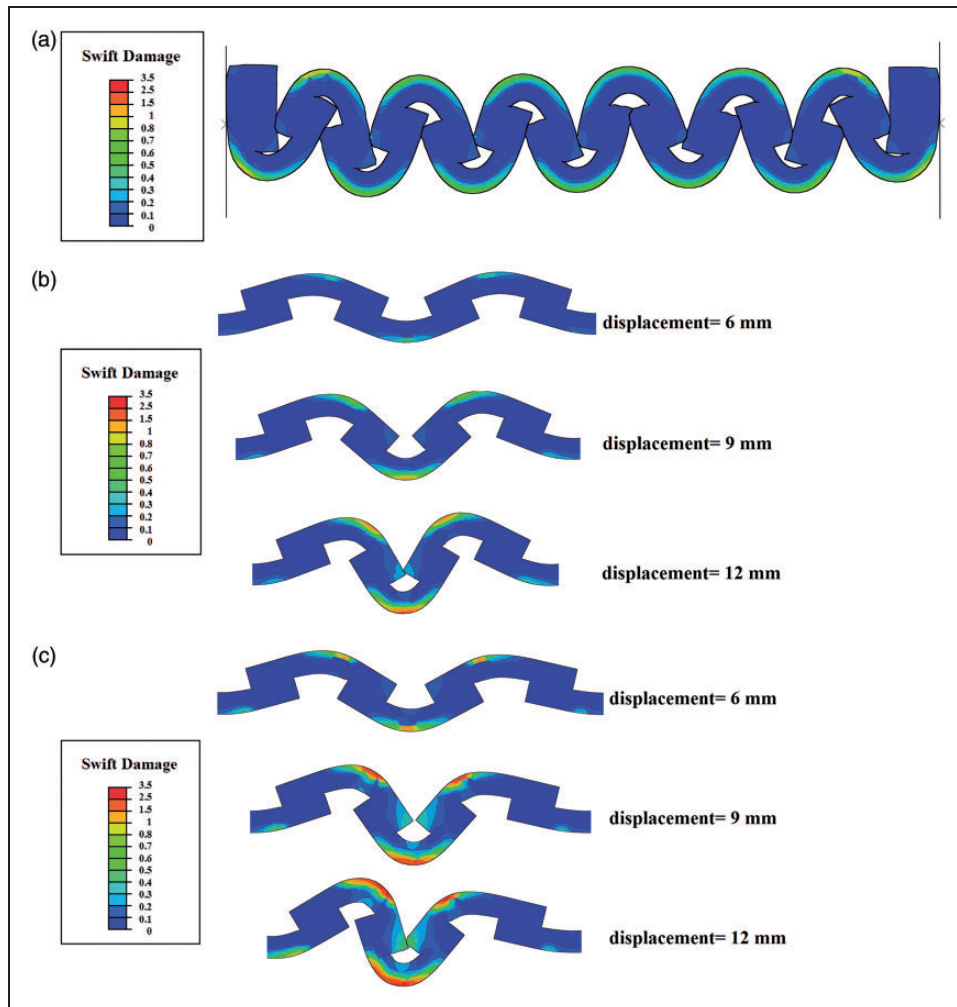
Figure 10. Comparison of swift damage criterion in: (a) F10 specimen; (b) F20 specimen; (c) F80 specimen.

1 after 6 mm of displacement as shown in Figure 10(c). This explains the overall fracture of F80 specimen during axial compression shown in Figure 5(b) and (c). This also describes the impressive decrease of compression load after little displacement shown in Figure 6(f). By comparing these results, it can be concluded that the fracture of specimens during axial compression can be predicted using Swift criterion.

Conclusions

Considering the results of this work, it can be concluded that:

1. Age hardening of tube results in increase of average load during axial compression. However, it may cause flow localization and fracture of tube.
2. Considerable energy absorption, reasonable load domain, and safe deformation with no macroscopic crack during axial compression can be obtained using moderated aging treatment. In this study, F10 specimen shows the optimum characterizations for energy absorbing elements.

3. The fracture of thin-walled tube during axial compression can be predicted using the Swift criterion. As a result, FEM simulation can be used not only to evaluate the compression load, but also to predict the fracture during axial compression.

References

1. Johnson W and Reid SR. Metallic energy dissipating systems. *Appl Mech Rev* 1978; 31: 277–288.
2. Majumder A, Altenhof W, Vijayan V, et al. Quasi-static axial cutting of AA6061 T4 and T6 round extrusions. *Proc IMechE, Part L: J Materials: Design and Applications* 2008; 222: 183–195.

3. Salehghaffari S, Tajdari M and Mokhtarnezhad F. The collapse of thick-walled metal tubes with wide external grooves as controllable energy-dissipating devices. *Proc IMechE, Part C: J Mechanical Engineering Science* 2009; 223: 2465–2480.

4. Alghamdi AAA. Collapsible impact energy absorbers: An overview. *Thin-Walled Struct* 2001; 39: 189–213.

5. Schneider F and Jones N. Impact of thin-walled high-strength steel structural sections. *Proc IMechE, Part D: J Automobile Engineering* 2004; 218: 131–158.

6. Singace AA and El-Sobky H. Uniaxial crushing of constrained tubes. *Proc IMechE, Part C: J Mechanical Engineering Science* 2001; 213: 353–364.

7. Shakeri M, Mirzaeifar R and Salehghaffari S. New insights into the collapsing of cylindrical thin-walled tubes under axial impact load. *Proc IMechE, Part C: J Mechanical Engineering Science* 2007; 221: 869–885.

8. Andrew KRF, England GL and Ghani E. Classification of the axial collapse of cylindrical tubes under quasi-static loading. *Int J Mech Sci* 1983; 25: 687–696.

9. Reid SR. Plastic deformation mechanisms in axially compressed metal tubes used as impact energy absorbers. *Int J Mech Sci* 1993; 35: 1035–1052.

10. Mamalis AG, Manolakos DE, Viegelahn GL, et al. The extensional collapse of grooved thin-walled cylinders of PVC under axial loading. *Int J Impact Eng* 1986; 4: 41–56.

11. Mamalis AG, Manolakos DE, Viegelahn GL, et al. Experimental investigation into axial plastic collapse of steel thin-walled grooved tubes. *Int J Impact Eng* 1986; 4: 117–126.

12. Mamalis AG, Manolakos DE, Viegelahn GL, et al. Energy absorption and deformation modes of thin PVC tubes: Internally grooved tubes when subjected to axial plastic collapse. *Proc IMechE, Part C: J Mechanical Engineering Science* 1989; 203: 1–8.

13. Gupa NK and Gupta SK. Effect of annealing, size and cut-outs on axial collapse behavior of circular tubes. *Int J Mech Sci* 1993; 35: 597–611.

14. Hosseinipour SJ and Daneshi GH. Experimental studies on thin-walled grooved tubes under axial compression. *J Exp Mech* 2004; 44: 101–108.

15. Hosseinipour SJ and Daneshi GH. Energy absorption and mean crushing load of thin-walled grooved tubes under axial compression. *Thin-Walled Struct* 2003; 41: 31–46.

16. Williams BW, Oliveira DA, Simha CHM, et al. Crashworthiness of straight section hydroformed aluminum tubes. *Int J Impact Eng* 2007; 34: 1451–1464.

17. Williams BW, Simha CHM, Abedrabbo N, et al. Effect of anisotropy, kinematic hardening, and strain-rate sensitivity on the predicted axial crush response of hydroformed aluminium alloy tubes. *Int J Impact Eng* 2010; 37: 652–661.

18. Bouchet J, Jacquelin E and Hamelin P. Dynamic axial crushing of combined composite aluminium tube: The role of both reinforcement and surface treatments. *J Compos Struct* 2002; 56: 87–96.

19. Bouchet J, Jacquelin E and Hamelin P. Static and dynamic behavior of combined composite aluminum tube for automotive applications. *J Compos Sci Technol* 2000; 60: 1891–1900.

20. Aktay L, Kroplin BH, Toksoy AK, et al. Finite element and coupled finite element/smooth particle hydrodynamics modeling of the quasi-static crushing of empty and foam-filled single, bitubular and constraint hexagonal- and square-packed aluminum tubes. *J Mater Des* 2008; 29: 952–962.

21. Kavi H, Toksoy AK and Guden M. Predicting energy absorption in a foam-filled thin-walled aluminum tube based on experimentally determined strengthening coefficient. *J Mater Des* 2006; 27: 263–269.

22. Kazeminezhad M and Hosseini E. Modeling of induced empirical constitutive relations on materials with FCC, BCC, and HCP crystalline structures: severe plastic deformation. *Int J Adv Manuf Tech* 2010; 47: 1033–1039.

23. Abaqus. *Analysis User's Manual, vol. 3, Part 23: Progressive damage and failure*. April 2011.

24. Pogatscher S, Antrekowitsch H, Leitner H, et al. Mechanisms controlling the artificial aging of Al–Mg–Si Alloys. *Acta Mater* 2011; 59: 3352–3363.

25. Swift HW. Plastic instability under plane-stress. *J Mech Phys Solid* 1952; 1: 1–18.